

Ultrafast X-ray diffraction measurements of shock-compressed iron and iron alloys

Andrew Krygier (✉ krygier1@llnl.gov)

Lawrence Livermore National Laboratory <https://orcid.org/0000-0001-6178-1195>

Marion Harmand

Institute of Mineralogy, Materials Physics and Cosmochemistry

Bruno Albertazzi

Laboratoire pour l'Utilisation des Lasers Intenses

Emma McBride

European X-Ray Free Electron Laser

Kohei Miyanishi

Institute for Laser Engineering, Osaka, Japan

Daniele Antonangeli

Sorbonne Université, Museum National d'Histoire Naturelle, UMR CNRS 7590

Yuichi Inubushi

Japan Synchrotron Radiation Research Institute

Ryosuke Kodama

Japan Synchrotron Radiation Research Institute

Michel Koenig

Laboratoire LULI

Takeshi Matsuoka

Osaka University

Gabriele Moggi

Sorbonne Université, Museum National d'Histoire Naturelle, UMR CNRS 7590

Fabio Pietrucci

Pierre and Marie Curie University

Marco Saitta

Uni Sorbonne

Tadashi Togashi

RIKEN

Yuhei Umeda

Osaka University

Tommaso Vinci

Laboratoire pour l'Utilisation des Lasers Intenses <https://orcid.org/0000-0002-1595-1752>

Makina Yabashi

RIKEN SPring-8 Cetner <https://orcid.org/0000-0002-2472-1684>

Toshinori Yabuuchi

RIKEN <https://orcid.org/0000-0003-0638-7640>

G. Fiquet

Sorbonne University

Norimasa Ozaki

Osaka University <https://orcid.org/0000-0002-7320-9871>

Article

Keywords: Ultrafast, X-ray diffraction, measurements of shock-compressed iron, iron alloys

Posted Date: August 17th, 2020

DOI: <https://doi.org/10.21203/rs.3.rs-52002/v1>

License:   This work is licensed under a Creative Commons Attribution 4.0 International License.

[Read Full License](#)

Ultrafast X-ray diffraction measurements of shock-compressed iron and iron alloys

A. Krygier^{1,2*}, M. Harmand¹, B. Albertazzi³, E. E. McBride^{4,5}, K. Miyanishi^{6,7}, D. Antonangeli¹, Y. Inubushi^{7,8}, R. Kodama^{6,9}, M. Koenig^{3,9}, T. Matsuoka¹⁰, G. Moggi¹, F. Pietrucci¹, A. M. Saitta¹, T. Togashi^{7,8}, Y. Umeda⁹, T. Vinci³, M. Yabashi^{7,8}, T. Yabuuchi^{7,8}, G. Fiquet¹, and N. Ozaki^{6,9}

¹Sorbonne Université, Muséum National d'Histoire Naturelle, UMR CNRS 7590, Institut de Minéralogie, de Physique des Matériaux, et de Cosmochimie (IMPMC), 75005 Paris, France

²Lawrence Livermore National Laboratory, 7000 East Ave, Livermore, CA 94550, USA

*krygier1@llnl.gov

³LULI, CNRS, CEA, Sorbonne Université, Ecole Polytechnique, Institut Polytechnique de Paris, F-91120 Palaiseau cedex, France

⁴European XFEL GmbH, Holzkoppel 4, D-22869 Schenefeld, Germany

⁵SLAC National Accelerator Laboratory, 2575 Sand Hill Road, MS 19, Menlo Park, California 94025, USA

⁶Institute for Laser Engineering, Osaka University, Suita, Osaka 565-0871 Japan.

⁷RIKEN Spring-8 Center, Sayo, Hyogo 679-5148 Japan

⁸Japan Synchrotron Radiation Research Institute, Sayo, Hyogo 679-5198, Japan

⁹Graduate School of Engineering, Osaka University, Suita, Osaka 565-0871 Japan.

¹⁰Open and Transdisciplinary Research Initiatives, Osaka University, Suita, Osaka 565-0871 Japan.

ABSTRACT

The extreme pressures achievable with dynamic compression holds great promise for studying planetary interiors. Phase stability of Fe-Si alloys, which are complex to address, is particularly relevant to understanding telluric planetary cores due to the widely varying properties produced by small changes in Si concentration. Here we report the study of phase stability of pure iron and Fe-Si alloys by x-ray diffraction measurements carried out on shocked samples using an x-ray free electron laser (XFEL). Our setup combined with the brilliance of the XFEL allows us to observe the rapid onset of high-pressure solid-solid phase transformation in Fe and Fe-Si_{8.5wt%}; we observe no such evidence in Fe-Si_{16wt%} up to 110 GPa on the nanosecond timescale. Density Functional Theory calculations provide the conceptual framework to rationalize these observations. Taken together our experiments and calculations support recent dynamic compression measurements and shed light on conflicting static compression results. Our work highlights the need to properly consider the differing intrinsic timescales of the static and dynamic experiments when comparing results, and the complementarity of the techniques in assessing phase diagram and transition mechanisms.

The interior of Earth and other rocky planets and exoplanets comprises a metallic core surrounded by a silicate mantle and a comparatively thin crust. Seismological and geodetic measurements of the Earth find that its core's average mass density is consistent with a high fraction of iron alloyed with lighter elements such as Si, S, O, C, and H^{1,2}. Many geophysical and geochemical arguments support the presence of Si within the core, with proposed abundances ranging from less than 1-2% up to ~10% by weight^{1,3-8}, with the density of the solid inner core best matched for Si content around 5 wt%. Models suggest that even higher Si concentration might exist at the core-mantle boundary⁹⁻¹¹ (135 GPa and ~4000 K). Like Earth, Mercury's core also comprises Fe alloyed with light elements, with the more reducing conditions during accretion yielding Si and S abundances potentially approaching 20%¹²⁻¹⁵. Finally, there are now

more than 4000 confirmed exoplanets¹⁶, with many more **detections expected** in the near future. The mass-radius relationship of many of these bodies implies similar bulk composition as Earth but permits a wide range of alloys¹⁷. Such expected compositional diversity motivates investigation of a wide range of materials including iron-based alloys across a broad spectrum of **thermodynamic** conditions.

The compositional dominance of iron in telluric core models and its **ready** availability for studies have motivated and enabled much work investigating the properties of pure iron^{18–21}. However, **even small amounts of alloy components in iron can** dramatically alter physical properties and phase relations²². For example, the addition of Si is suggested to stabilize cubic phases over a large pressure and temperature range^{6;23–25}, at the expense of the hexagonally-close-packed ϵ -phase formed by pure iron at high pressure. Furthermore, there are many forms of steel with widely varying properties determined by their precise composition. This leaves many open questions regarding the cores of rocky planets. For example, the elastic anisotropy and strength of the constituting material²⁶ is one explanation for Earth's inner core seismic wave anisotropy^{27–29}, **and these mechanical properties clearly depend upon the** crystalline structure^{19;30–32}. The high-pressure melt curve and magnetism are other important properties also strongly influenced by the crystalline structure and composition.

Phase relations and equations of state have been proposed for a wide range of Fe-Si alloys based off of x-ray diffraction (XRD) measurements using diamond anvil cells (DAC) and Laser Heated Diamond Anvil Cell (LH-DAC)^{6;23;25;33–35}. Hirao et al.³³ report the transformation from ambient body-centered-cubic (bcc) to hcp over the pressure range ~ 16 -35 GPa in Fe-Si_{8.7wt%} and stability of the cubic phase up to ~ 124 GPa in Fe-Si_{17.8wt%}, at 300 K. Fischer et al.²³ report the transformation from cubic to pure hcp-phase in Fe-Si_{9wt%} around 45 GPa and 1400 K, and suggest a phase boundary at about 20 GPa and 1000 K, with a mixture of B2-hcp stable at higher temperature, up to melting. Fischer et al.⁶ report the transformation from cubic B2 or D0₃ phase to mixed B2-hcp phase for Fe-Si_{16wt%} above 50 GPa at 1000 K, with a positive Clausius-Clapeyron slope. Edmund et al.²⁵ report **on the dependence** of the bcc-hcp phase transition pressure with Si content, with the transition pressure at 300 K increasing by ~ 11.5 GPa per wt% Si between ~ 8 -12 wt% Si, and no observation of the hcp phase for Fe-Si_{17wt%} up to ~ 65 GPa. However, despite the numerous studies, the phase diagrams of Fe-Si alloys remain controversial.

While the range of pressures and temperatures accessible with LH-DAC continues to increase^{18;36}, achieving Earth inner core-like conditions remains extremely challenging as these conditions approach the compressive strength of diamond at room temperature. Other factors can also undermine the efficacy of this technique. For example, diffusive contamination of carbon from the anvil can form unintended alloys, in particular at high temperature^{18;37}, and significantly change physical properties and phase stability. De-mixing of alloy samples into regions of different composition can occur due to pressure and temperature-induced solubility changes and divariant phase transitions^{38;39}. Large temperature gradients can also trigger sample de-mixing. Additionally, statically compressed iron tends to display a preferred orientation where the basal plane is aligned with the face of the diamond anvils, with deviatoric stress imposing lattice distortions⁴⁰.

Dynamic compression by laser ablation can achieve much higher pressures and temperatures than LH-DAC and also has specific comparative advantages. For example, Wicks et al.²⁴ have recently explored the phase relations in Fe, Fe-Si_{7wt%} and Fe-Si_{15wt%} up to 1300 GPa using ramped-wave loading combined with nanosecond XRD. **Unlike Fischer²³, they do not observe a phase transformation in Fe-Si_{15wt%} and note that it may be due to the low temperatures achieved using the ramp compression technique or the short timescale preventing dissociation into Si-rich B2 and Si-poor hcp.** Samples in laser-compression experiments like these are subject to strain rates approaching 10^9 s⁻¹ that endure for times on the order of ~ 1 -10 nanoseconds. **While the initial strain is uniaxial, some combination of plasticity, phase transformation, and twinning relieve the resulting shear strain and the sample rapidly**

becomes approximately hydrostatic. This approach ensures precise knowledge of the *in-situ* sample composition at the nanosecond timescale and gives access to phenomena like high-pressure crystalline phase transformation kinetics^{20;21;41;42}. For example, Smith et al.²⁰ and Amadou et al.²¹ have inferred that the bcc-hcp transformation occurs **in pure Fe** on a timescale of ~ 1 ns, consistent with a nucleation and growth process. They also find a higher transformation onset stress than reported using static compression. On the other hand, kinetics in non-metals can occur on much longer timescales^{43;44}. Recent measurements have also observed phase transformation boundary lowering in dynamic compression^{45;46}. The application of dynamic compression experiments to the determination of stable phase relations for systems of geophysical interest holds great potential but is not as straight-forward as it might appear.

Here, we explore the phase stability of iron, Fe-Si_{8.5wt%} and Fe-Si_{16wt%} in conditions near those existing at the Earth's core-mantle boundary using laser-driven shock wave compression. We investigate the cubic phase stabilization of iron alloys for increasing Si content and compare approaches in a pressure-temperature regime previously explored with LH-DAC **and at higher temperature than studied with dynamic compression. Our ultrafast structural measurements of shocked samples, which for the same pressure generate higher entropy and therefore temperature than in ramp compression, help further understanding about the origins of this disagreement.**

X-ray free electron laser (XFEL) sources now provide bright enough x-ray beams to record high-quality XRD measurements in a single, femtosecond-scale pulse making a wide range of new studies possible. We have used the extremely bright, ~ 10 fs x-ray pulse generated at the Spring-8 Angstrom Compact Free Electron Laser⁴⁷⁻⁴⁹ (SACLA) facility in Japan to determine the crystal structure during the initial shock in Fe, Fe-Si_{8.5wt%}, and Fe-Si_{16wt%} as well as on release into sapphire in Fe-Si_{16wt%}. The short duration and high brightness of the x-ray pulse combined with the short penetration depth of the x-rays in the reflection probe geometry allows us to effectively take snapshots of the crystallographic phase. We have observed the rapid onset of the hcp phase but not completion of the transformation in Fe and Fe-Si_{8.5wt%} during the initial shock. On the other hand, we observe no evidence of a structural phase transformation in Fe-Si_{16wt%} either during the initial shock or on release, which is in disagreement with the prevailing view coming from early static measurements^{6;23}. Our new measurements were only possible with the combination of XFEL pulse, reflection geometry as shown in figure 1, and exploiting textured samples.

Results

Direct laser ablation forms an expanding surface plasma that drives our samples to high pressure. The expansion causes the target to recoil, which generates a pressure wave that travels into the sample away from the ablating surface, forming a shock. On some shots, the VISAR diagnostic monitored Fe/sapphire interface motion – the inset in Fig. 1 shows example data. Figure 2 shows integrated XRD patterns of ambient (dashed green line) and *in situ* high-pressure (solid purple line) of Fe (a), Fe-Si_{8.5wt%} (b), and Fe-Si_{16wt%} (c) recorded during the initial shock. Labels give the phase and reflection plane of each observed peak; asterisks denote the high-pressure phase peaks. We describe the identification process for each of the reflections in detail below. Fe and Fe-Si_{8.5wt%} patterns include reflections from a ~ 100 nm deposition of Au used to aid sample alignment (see Methods), which prevented VISAR collection when fielded.

On shots where VISAR was available, we determine pressure using impedance matching between the iron and sapphire window⁵⁰. Comparing the observed peak particle velocity and breakout time to simulations using the 1D radiation hydrodynamics code MULTI⁵¹ helps to confirm the pressure regime. The presented data are all measured for the same laser intensity and sample design. In general, the

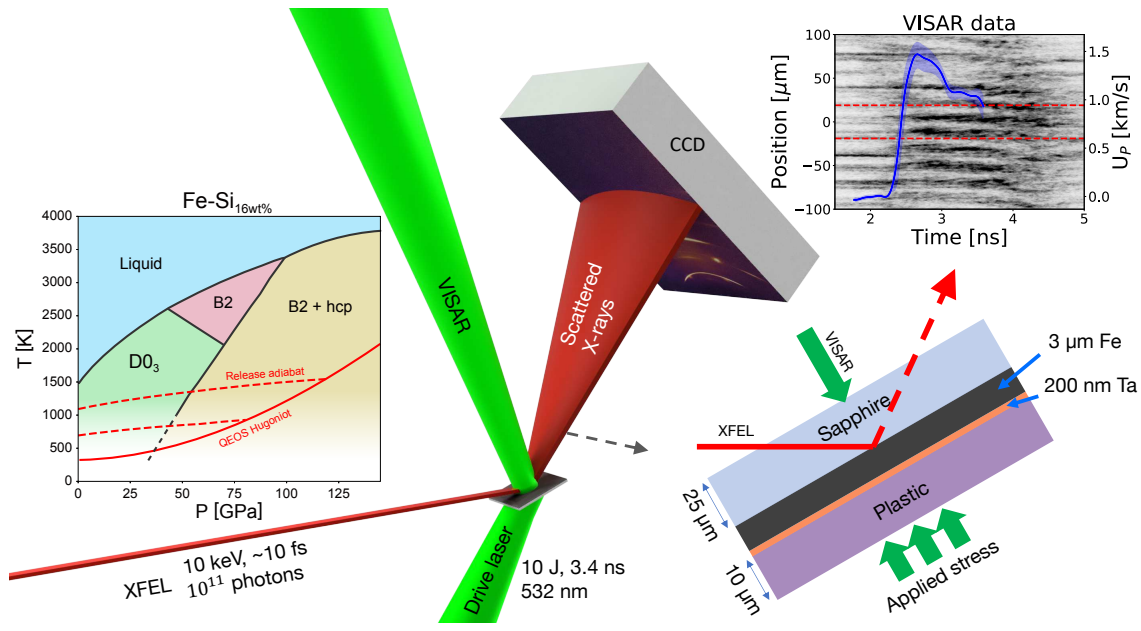


Figure 1. The experimental setup and sample VISAR data. A CCD detector located 76 mm from the interaction point and covering the range $2\theta_B = [17^\circ:100^\circ]$ collects scattered x-rays. The sandwich sample layers, shown in the bottom right, are $10 \mu\text{m}$ CH / 200 nm Ta / $3 \mu\text{m}$ Fe / $25 \mu\text{m}$ sapphire. On some shots, there was an additional 100 nm Au layer on the Sapphire window. The top right inset shows sample VISAR data with the XFEL probe region highlighted in dashed lines. The shaded region in the VISAR data shows the statistical standard deviation of the velocity. The inset to the left shows the Fe-Si_{16wt%} phase diagram from Fischer²³ with the shock Hugoniot and example QEOS release adiabat.

pressures inferred from VISAR measurements and with MULTI agree with the pressure inferred using an equation of state^{6:33:52} for the volume measured by the x-ray diffraction. We do not see the typical multi-wave behavior associated with the bcc-hcp transformation due to the higher velocity of the hcp phase. This is due to the strength of the shock and prevents use of typical wave-profile analysis to determine phase transformation kinetics, instead requiring a direct structural probe like XRD. Across our data, the rise time of the shock is observed to be $0.5 \pm 0.1 \text{ ns}$, which combined with the directly measured strain gives an average strain rate of $\dot{\epsilon} = 1.5 \pm 0.3 \times 10^8 \text{ s}^{-1}$ ($\epsilon = \frac{d_0 - d}{d_0}$, where d_0 and d are the ambient and compressed d -spacings, respectively).

Table 1 summarizes the reflections observed in the data shown in Fig. 2. The volume calculation assumes hydrostatic compression (for both cubic and hcp phases) and a c/a ratio of 1.61 for the hcp phase, as found by other laser-shock experiments⁵³ and close to the value reported by static studies⁵⁴. The data in Fig. 2 were collected during the initial shock, i.e., along the principal Hugoniot. For Fe-Si_{16wt%} we have also performed additional shots at various pressures ranging from $\sim 10 - 110 \text{ GPa}$ both on the initial shock and after breakout into sapphire and find no evidence of phase transformation.

Phase Identification

As seen in Fig. 3 (a), the preferred orientation of crystallites (texture, due to the deposition process) in our Fe samples produces azimuthally narrow XRD spots. This is in contrast to the typical (azimuthally broad) Debye-Scherrer rings associated with XRD from powder samples with no texture like the Au reflections seen in Fig. 3 (b) and (c). While the geometry, sample texture, and detector size prevent observation of some reflections, the azimuthally narrow XRD spots arising from our textured samples make it possible to

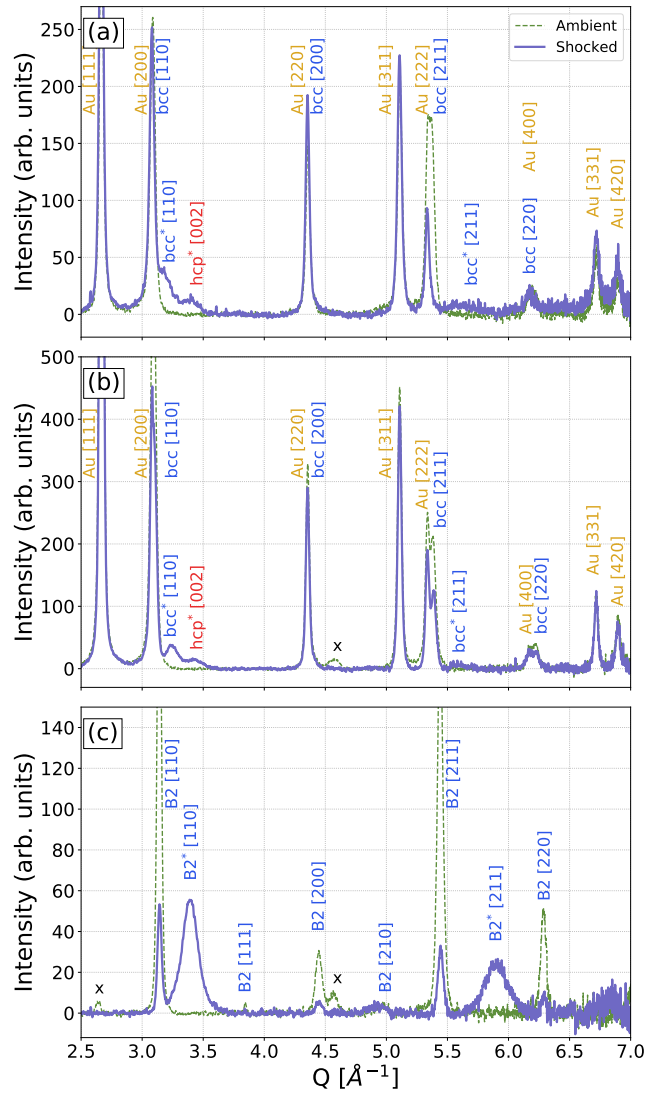


Figure 2. Azimuthally integrated diffraction patterns of shocked Fe (a), Fe-Si_{8.5wt%} (b), and Fe-Si_{16wt%} (c). Upon compression, Fe and Fe-Si_{8.5wt%} form a mixture of bcc and hcp phases, respectively. Our data shows that Fe-Si_{16wt%} stays in the cubic phase. The black x symbol in (b) and (c) indicates reflections from the sample holder. We have masked out reflections from the single crystal sapphire.

Table 1. Summary of diffraction reflections, corresponding phase, and volume.

Sample	phase	reflection	Q [\AA^{-1}]	v/v ₀
Fe	bcc	{110}	3.19 (0.03)	0.912 (0.026)
		{211}	5.57 (0.08)	
	hcp	{002}	3.42 (0.05)	0.705 (0.031)
Fe-Si _{8.5wt%}	bcc	{110}	3.24 (0.03)	0.897 (0.024)
		{211}	5.59 (0.06)	
	hcp	{002}	3.44 (0.04)	0.698 (0.025)
Fe-Si _{16wt%}	B2	{110}	3.40 (0.06)	0.787 (0.042)
		{211}	5.88 (0.11)	

exploit the known orientation relationship between the bcc and hcp phases^{55;56}. This technique^{57;58} holds great power for understanding the high-pressure evolution of the crystalline structure in solids and great potential for studying phase transformation mechanisms and kinetics.

Fe and Fe-Si_{8.5wt%}

Figure 3 (a) and (b) show raw diffraction measurements from ambient and compressed Fe, respectively. The textural similarity between the ambient and high-pressure diffraction is the key to our analysis. The high-pressure bcc {110} and {211} reflections in Fig. 3 (b) have the same pattern as their ambient counterparts in (a) and yield the same bcc lattice parameter to within $\sim 1\%$, smaller than the uncertainty of the measurement. We identify the hcp {002} reflection (red in Fig. 3 (b)) by combining knowledge of the initial bcc texture and *a priori* knowledge of the parent-child orientation relationship, addressed by both static and dynamic compression XRD experiments. In these descriptions the bcc {110} becomes the hcp {002} plane while maintaining its initial orientation. This relationship combined with their similar *d*-spacings for our pressure produces the similar azimuthal bcc {110} and hcp {002} diffraction patterns we observe. Furthermore, as already mentioned, identifying this reflection as the hcp {002} and assuming a *c/a* ratio of 1.61, in line with other measurements in shocked samples, gives a volume consistent with our MULTI simulations and VISAR data from other shots. Sample texture and/or being below the detection threshold explains the absence of hcp {100} and {101} reflections.

The Fe-Si_{8.5wt%} samples (shown in Fig. 3 (c)) do not have the same texture as the Fe samples, but they have a similar level of agreement between the bcc {110} and {211} reflections as seen in Fig. 2 (b), and so we interpret the three observed lines in the same way.

Fe-Si_{16wt%}

The Fe-Si_{16wt%} samples form the B2 structure at ambient conditions. Fischer et al.⁶ report the D0₃ structure at ambient conditions in samples with similar Si content. However, the D0₃ and B2 phases are structurally alike and produce similar diffraction patterns with D0₃ producing a few additional very weak reflections that may have been below our detection threshold. Furthermore, physical vapor deposition synthesis at relatively low temperature does not favor Si ordering^{25;59}. The inset in Fig. 1 shows the Fe-Si_{16wt%} phase diagram, reproduced from Fischer et al. with the shock Hugoniot and example release adiabats (calculated using QEOS⁶⁰) for Fe-Si_{16wt%}. Based on the results from Fischer, we expected to see a mixture of B2 + hcp in the conditions of our experiment.

We find no evidence of a structural phase transformation during the initial shock over a range of pressures (~ 10 -110 GPa) or upon release from high pressure. The lack of some of the weaker reflections at

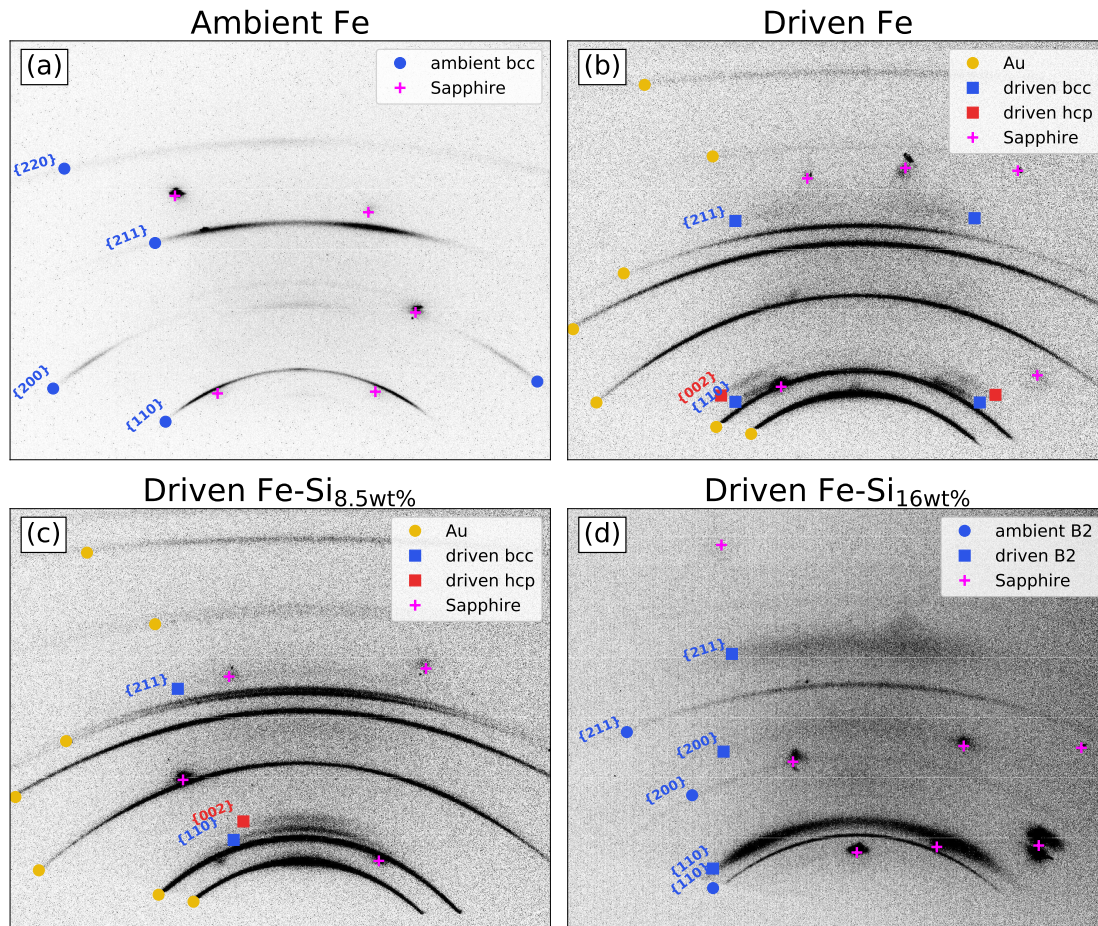


Figure 3. Raw diffraction images of ambient Fe (a), driven Fe (b), driven Fe-Si_{8.5wt%} (c), and driven Fe-Si_{16wt%} (d) with phases identified. The driven images correspond to the integrations shown in figure 2 and described in the text. Circles and squares indicate ambient and high-pressure reflections, respectively. Gold circles indicate Au reflections in (b) and (c); pink pluses indicate single crystal sapphire reflections. Blue and red markers indicate cubic (bcc/B2) hcp phase reflections blue and red, respectively. The ambient Fe image (a) clearly shows the initial sample texture; in (b) the Au obscures the ambient texture. The Debye-Scherrer rings form ellipses due to the geometry (see Fig. 1); the diffuse background is likely due to X-rays generated in the front-surface laser ablation and fluorescence from the XFEL interacting with the Au layer.

high-pressure is due to the background and noise generated by the ablation plasma, **but does not invalidate our conclusions**: we cannot distinguish bcc from B2 or D0₃ (going forward all references to the B2 phase have this caveat) **but we can clearly discard the presence of the hcp phase**.

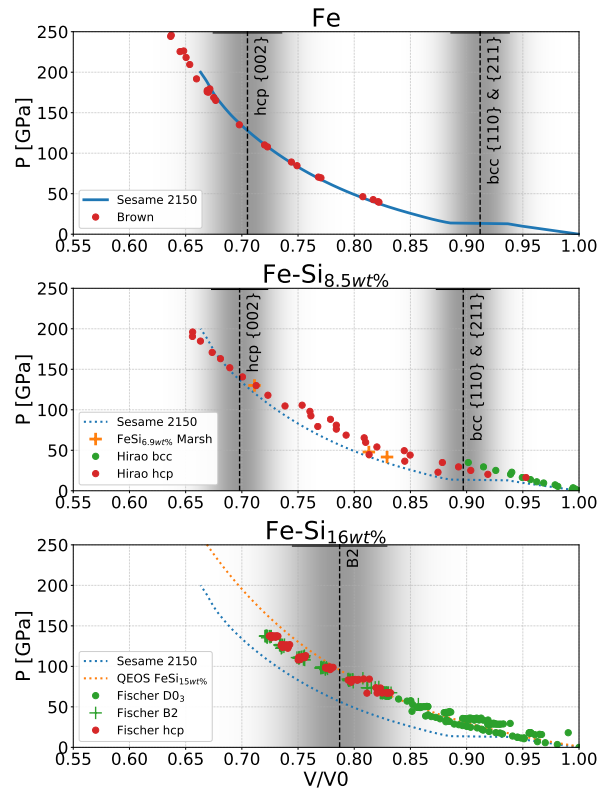


Figure 4. Pressure-volume relations for Fe, Fe-Si_{8.5wt%}, and Fe-Si_{16wt%} plotted with similar alloys. The black lines/gray shading show volume and uncertainty of our measurements. Comparative Hugoniot/static data: in (a), the Sesame 2150 calculated shock Hugoniot is plotted with shock Hugoniot data from Brown et al.⁵²; in (b), static compression phase relation data for Fe-Si_{8.7wt%} from Hirao et al.³³ taken at 300 K and shock Hugoniot data for Fe-Si_{6.9wt%} from Marsh et al.⁶¹ are plotted; in (c), static compression data for Fe-Si_{16wt%} from Fischer et al.²³ heated between 300-2200 K. Panels (b) and (c) also show the Sesame 2150 shock Hugoniot for comparison.

Discussion

The advent of laser-driven dynamic compression has vastly expanded the range of accessible pressure and temperature conditions. However, the intrinsically high strain-rate and uniaxial strain can activate exotic material responses like strain-rate dependence of phase boundaries **and large flow stress**. While wave profile analysis can investigate dynamic effects like these^{20;21}, the approach lacks direct, simultaneous phase determination. **Recent dynamic compression studies using XRD have found different phase boundaries than in static compression^{45;46}**, which ultimately raises questions about the applicability of dynamic compression to the study of equilibrium phase diagrams of interest in Earth and planetary science. Identifying and understanding these kinds of disagreements in conditions already studied with static compression is therefore imperative. This careful approach is fundamental to developing any new technique and obviously needed for dynamic compression.

The ultrafast x-ray pulse combined with the reflection geometry allows extremely high temporal resolution. In our setup, the rearmost 1 μm of the sample (x-ray side) scatters $\sim 64\%$ of the detected x-rays. This depth corresponds to ~ 130 ps in shock transit time of flight in our conditions. **The x-ray pulse probes the sample before the initial shock transit is complete - any compressed signal is therefore probing the leading edge of the shock.** This effectively sets an upper bound of ~ 130 ps on the timescale for the onset of the bcc-hcp phase transformation in iron **and Fe-Si_{8.5wt%} under these conditions.** This time resolution allows us to confirm the differences observed between static and dynamic compression from Fischer et al.²³ and Wicks et al.²⁴ as well as suggesting preliminary insight into the origin of these differences.

We have observed both the transient bcc and high-pressure hcp phase in pure iron during the initial shock, **a result of the transient compression dynamics.** However, **the nature of strain relaxation in dynamic compression is largely undetermined.** A series of large computer simulations of the behavior of polycrystalline and single crystal iron by Kadau et al.^{62:63} give insight into these dynamics. They propose that the compression process starts with initial elastic compression, followed by plastic deformation in the bcc phase, and finally transformation into the high-pressure hcp phase. **Our data simultaneously visualizes the transiently compressed bcc phase and the transformed high-pressure hcp phase.** The d -spacing of the transient, compressed iron bcc phase corresponds to a hydrostatic pressure of 19.1 ± 6.6 GPa (Sesame 2150), though the conditions inside the shock front are by definition far from equilibrium and may have high strain anisotropy. The $\{002\}$ hcp phase d -spacing corresponds to a hydrostatic pressure of 128 ± 35 GPa. The pressure of the final state is well above the expected hcp onset stress determined by Smith et al. ($\sigma_{\alpha \rightarrow \epsilon} = 1.15 \times \dot{\epsilon}^{0.18}$) that evaluates to 34 GPa in our conditions, and so we would expect to observe hcp. The behavior of the initial compression remains an open and interesting question for future, tailored dynamic compression studies.

This highlights the importance of investigating phase transformation dynamics in compression experiments before applying these results to constrain phase diagrams. As well, our work clearly shows the advantage of using textured samples for this purpose. This approach could be especially useful for identifying phase transformation orientation relationships, or for resolving uncertainties in ambiguous diffraction data. Performing this experiment with a powder sample could have hypothetically led one to mistakenly interpret the driven bcc $\{110\}$ reflection as the hcp $\{100\}$ plane. This faulty assumption yields a c/a ratio of 1.64 for the hcp phase, significantly higher than observed in either dynamic⁵³ or static⁶⁴ experiments. As a non-ideal c/a ratio in the hcp structure could be related to elastic anisotropy, an incorrect assessment would lead, for instance, to **erroneous** conclusions concerning the seismological anisotropy exhibited by Earth's inner core^{27:28}.

As for the case of Fe, we have observed multiple phases during the initial shock in Fe-Si_{8.5wt%}. **The similarity of the data argues for the same interpretation and the same underlying phenomena.** The measured d -spacing of the **transient** bcc $\{110\}$ and $\{211\}$ **reflections** corresponds to a **hydrostatic** pressure of 38 GPa; the **high-pressure** hcp $\{002\}$ reflection corresponds to a pressure of 132 ± 26 GPa using the 300 K static compression equation of state from Hirao et al.³³. We make no thermal corrections since the Hirao data agrees well with the shock Hugoniot data reported in Marsh et al.⁶¹, as seen in Fig.4, for Fe-Si_{6.9wt%}; measurements of Fe-Si_{5wt%} at slightly lower pressure by Edmund et al.⁶⁵ suggest the thermal pressure is ~ 15 GPa for our conditions, similar to that found by Fischer et al. in Fe-Si_{16wt%} and less than our error bars. The inferred bcc pressure is consistent with our calculations for the transformation pressure described below. Given the rapid onset, the bcc-hcp phase transformation process in Fe-Si_{8.5wt%} is likely a non-diffusive process like the Martensitic bcc-hcp phase transformation in iron. Assuming the Clapeyron slope is positive, these results would seem to support our findings.

On the other hand, we observe no evidence for a phase transformation in Fe-Si_{16wt%}. These results are in disagreement with Fischer et al.⁶ Edmund et al.²⁵ have studied the bcc-hcp transformation onset

pressure over a range of Fe-Si alloy concentrations at ambient temperature. They find a slightly increasing hcp onset pressure up to 8.7wt% Si; the phase boundary then increases by ~ 11.5 GPa/wt% up to 11.8wt%, and the hcp phase in Fe-Si_{17wt%} is not observed up to 65 GPa. The reported absence of transition in Fe-Si_{17wt%} at 300 K up to 65 GPa, together with the positive Clapeyron slope of the transition, appear in contrast to the presence of hcp phase at 50 GPa and 1000 K argued by Fischer, and rather in agreement with our observations.

To supplement our measurements and provide further insight, we have performed structural prediction calculations using Density Functional Theory (DFT) at 0 K. The phase diagrams for Fe-Si_{9.1wt%} (Fe₁₀Si₂ cell) and Fe-Si_{16.7wt%} (Fe₁₀Si₄ or Fe₅Si₂ cells) were calculated for the pressure range between 0 and 120 GPa, by estimating the relative enthalpy of the main phases at the GGA-PBE level of approximation⁶⁶ for the exchange-correlation energy functional. These concentrations approximate the experimental conditions while managing the calculation size. Non-magnetic B2 and hcp phases use the larger Fe₁₀Si₄ cell, while ferromagnetic D0₃ uses the smaller Fe₅Si₂ cell due to the heavier computational cost of magnetic DFT calculations. The calculations aiming to predict the ferromagnetic phases include magnetic effects through the implementation of a standard basic collinear spin-polarization model. The Ab Initio Random Structure Search⁶⁷ (AIRSS) code was employed for performing crystal structure predictions, coupled with efficiency enhancements described in the Methods section and detailed in a separate publication⁶⁸.

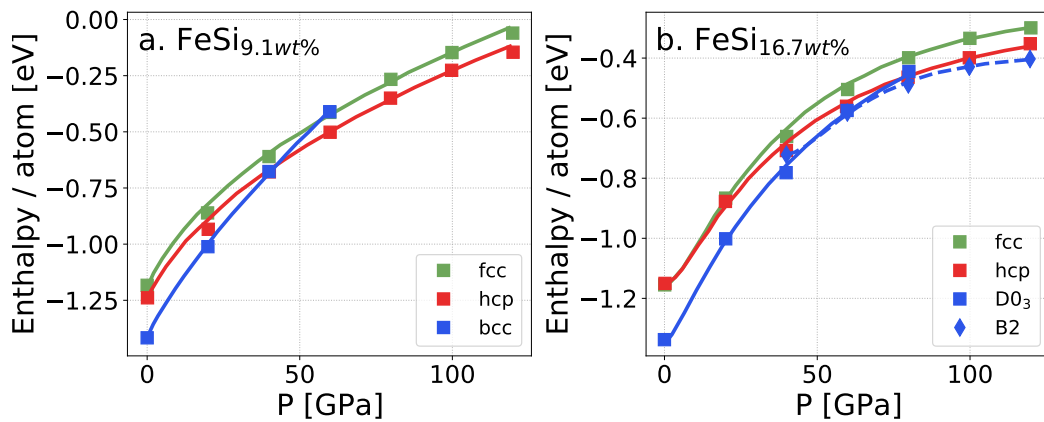


Figure 5. Phase stability calculations using density functional theory at 0 K for Fe-Si_{9.1wt%} (a) and Fe-Si_{16.7wt%} (b).

Figure 5 shows predictions of enthalpy vs. pressure from these calculations. The thermodynamically stable phase is the one with the structure having the lowest enthalpy. For Fe-Si_{9.1wt%}, the ferromagnetic bcc phase dominates at low pressures; we find hcp is most stable above ~ 40 GPa. In the case of Fe-Si_{16.7wt%}, the ferromagnetic D0₃ phase dominates at low pressures. Starting at ~ 60 GPa, the B2 phase stabilizes, with the hcp phase being slightly less stable than B2 by around 20-50 meV/atom. The fcc phase remains metastable at all pressures in both alloys. The increasing stabilization of the cubic phases for increasing Si concentration as seen in Fig. 5 agrees with previous results^{6,23–25;69} and our measurements that small differences in Si concentration impact phase stability. This also highlights a possible advantage of using laser-generated compression, which is largely immune to diffusive concentration changes due to the short timescale.

The different timescales of the experiments could also explain these apparent inconsistencies. Our findings are in agreement with Wicks et al.²⁴, suggesting that the process required to form the hcp phase observed by Fischer in Fe-Si_{16wt%} may not be active on the 1-10 nanosecond timescale. Static compression

experiments typically take place on timescales of at least seconds, which in principle eliminates transient effects, but also enables diffusion. Atomic rearrangement is common in shock waves as a result of, for example, plasticity (due to the large applied stress) and Martensitic phase transformations. However, dynamic compression occurs on a timescale that largely prevents diffusive processes that change bulk alloy concentrations like those used to form steels. Recent studies in other materials have revealed diffusive phase transformations active on timescales as fast as tens of nanoseconds using dynamic compression⁴³ and can evolve with characteristic times on the order of hundreds of seconds or more using static compression⁴⁴, highlighting a broad range of possible behaviors. In our case, the rapid stabilization of the hcp structure for iron and for Fe-Si_{8.5wt%}, but not for Fe-Si_{16wt%}, may imply that in this latter case the formation of hcp phase may require non-Martensitic action **like diffusive de-mixing**.

Summary

We have **studied** phase relations in shocked Fe, Fe-Si_{8.5wt%}, and Fe-Si_{16wt%}. Using femtosecond XRD **measurements**, we have directly identified a transient mixture of bcc+hcp phases in the initial shock in Fe and Fe-Si_{8.5wt%}, which is a result of the kinetics of the bcc-hcp phase transformation. **Differently from early** static experiments^{6;23}, we see no evidence for a high-pressure phase transformation in Fe-Si_{16wt%} during either the initial shock or release. The different timescales of the experiments could explain this observation and may imply a different cubic-hcp phase transition mechanism for high Si concentrations. Finally, these results suggest that we could leverage the temporal and out-of-equilibrium aspects of laser shock compression to study phase stabilization processes and mechanisms in both Fe-Si alloys and other materials.

Acknowledgments

The XFEL experiments were performed at the BL3 of SACLA with the approval of the Japan Synchrotron Radiation Research Institute (proposal nos. 2015A8023, 2015A8066, 2015B8014, 2015B8063, and 2017A8062). This work is in part supported by the French Agence Nationale de la Recherche with the ANR IRONFEL 12-PDOC-0011, by the Japan Society for the Promotion of Science (JSPS) KAKENHI (grant nos. 16H01119 and 18H04368), JSPS core-to-core program on International Alliance for Material Science in Extreme States with High Power Laser and XFEL, the X-ray Free Electron Laser Priority Strategy Program at Osaka University from the Ministry of Education, Culture, Sports, Science, and Technology (contract no. 12005014), the Centre National de la Recherche Scientifique GoToXFEL program, and under the auspices of the Lawrence Livermore National Security, LLC, (LLNS) under Contract No. DE-AC52-07NA27344. This work was supported by the Department of Energy, Laboratory Directed Research and Development program at SLAC National Accelerator Laboratory, under contract DE-AC02-76SF00515 and as part of the Panofsky Fellowship awarded to E.E.M. This work was further supported by Fusion Energy Sciences FWP10018. This project has also received funding from the European Research Council (ERC) under the European Union's Horizon 2020 research and innovation program (grant agreement No. 670787 D PLANETDIVE). We thank I. Estève for assistance with the scanning electron microscopy and B. Baptiste for assistance with the laboratory X-ray diffraction, that both allowed full characterization of the initial samples. We would like to thank A. Benuzzi-Mounaix, E. Edmund, G. Morard, and C. Wehrenberg for helpful discussions and A. Faenov, T. Pikuz, and Y. Tange for supporting the project.

Author Contributions

A.K, M.H., R.K., M.K., M.Y., G.F., and N.O. conceived the project. A.K, M.H., B.A., E.E.M, Y.I., T.M., K.M., T.T., Y.U., T.Y., and N.O. performed the experiment. A.K., M.H., and G.F. analyzed and interpreted the experimental data. M.H. and T.V. performed hydrodynamic simulations. G.M., F.P., and A.M.S. performed the DFT calculations and analysis. A.K. and M.H. wrote the paper with input from D.A, G.F., G.M., F.P., and A.M.S and N.O. All authors contributed to the work presented here and to the final paper.

Methods

Experimental Details

We performed powder X-ray diffraction measurements of Fe, Fe-Si_{8.5wt%}, and Fe-Si_{16wt%} sandwich layered samples. A 10 μm Parylene-N layer is used as an ablator. A second 200 nm thick Ta layer, prevents pre-heating from the laser-ablator interaction. The $\sim 3 \mu\text{m}$ Fe(-Si_x) sample layer is deposited using physical vapor deposition directly onto the 25 μm thick c-cut single crystal sapphire layer, which is used as a tamper and VISAR window. In some samples, the VISAR-facing (rear) side of the sapphire window was coated with a ~ 100 nm thick Au layer, which was used as an alignment fiducial. The Au layer melts under direct XFEL exposure allowing precise coalignment of the optical drive laser and XFEL to the sample. The samples have been characterized by ambient diffraction performed using a Rigaku diffractometer and coupled ion polishing and SEM microscopy - a summary of these ambient properties is given in Table 2. Fe and Fe-Si_{8.5wt%} are observed to take the bcc structure under ambient conditions while Fe-Si_{16wt%} samples take the B2 structure as indicated by the presence of $\{111\}$ and $\{210\}$ reflections in addition to the bcc reflections.

Sample	ρ_0 [g/cm ³]	phase	Δz [μm]	Si wt%
Fe	7.86	bcc	3.0	–
Fe-Si _{8.5wt%}	7.37	bcc	2.7	8.5(5)
Fe-Si _{16wt%}	7.08	B2	2.9	16.0(2)

Table 2. Summary of sample initial conditions. The density is calculated from the weighted average of observed diffraction lines corresponding to the cubic phase. We observe no sign of C contamination.

High pressure was achieved dynamically via laser-generated shock wave using the EH5 end station at SACLA. Our samples were irradiated with ~ 10 J of 532 nm radiation in a 3.4 ns pulse focused with a lens to a $\sim 250 \times 500 \mu\text{m}^2$ spot projected onto the angled target plane. The laser was incident at an angle of $\sim 57^\circ$ from normal giving a target-plane irradiance of $\sim 1 \times 10^{12}$ W/cm². The laser interacts with the ablator layer, launching a shock wave into the sample; the difference in shock impedance at the CH and Ta interfaces causes a significant pressure increase in the Ta that propagates to the probe layer. Sapphire has similar shock impedance as Fe and is used to minimize wave reflections at the interface.

We probed the crystal lattice structure with X-ray diffraction by using the ~ 10 fs SACLA XFEL pulse, with 10^{11} photons/pulse tuned to 10.1 keV. Scattered X-rays were collected using a 3.2 megapixel CCD detector placed 76.6 mm from the interaction point with a vertical orientation as shown in figure 1. The sample was probed in a reflection geometry with the X-ray pulse incident on the rear surface at 20° from the sample surface. With respect to the geometry shown in figure 1, the X-ray pulse is slitted to 200 μm in the out of the page direction and focused with Kirkpatrick-Baez mirrors to 13 μm in the vertical direction, projecting to $\sim 38 \times 200 \mu\text{m}^2$ on the sample surface. The detector position is determined with CeO₂ powder diffraction; the detector position calibration and integrations were performed using Dioptas⁷⁰.

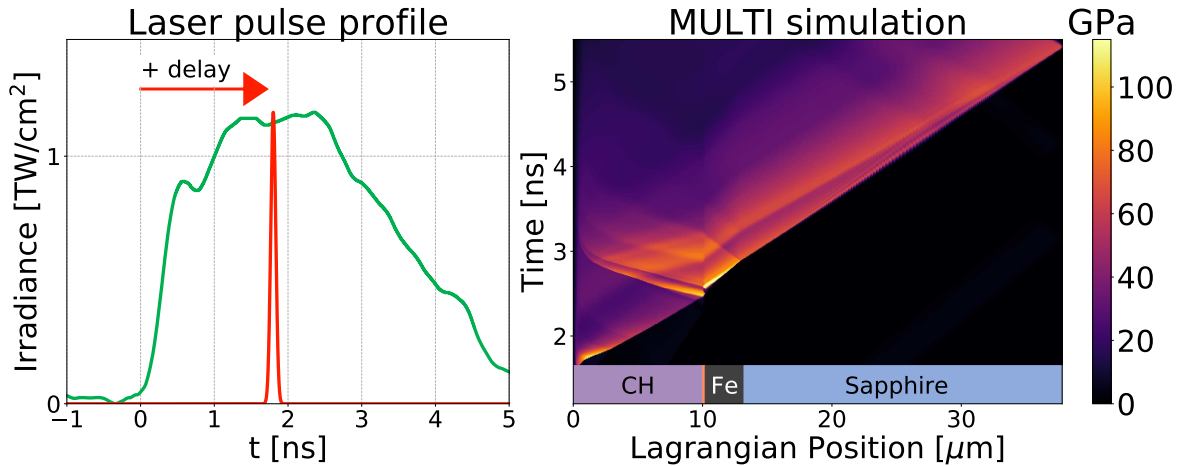


Figure 6. Experimental pulse shape (left panel) and MULTI hydrodynamics (right panel) simulation showing the pressure as a function of time and Lagrangian position. The peak irradiance is 8×10^{11} W/cm², which is lower than our experimental irradiance as typical of 1D radiation hydrodynamics simulations, produces the best fit to our data. The sample layers are indicated on the bottom (with the Ta heat shield included, but not labeled).

The reported uncertainty in reflection positions is determined by the width of the best-fit Gaussian to the deconvolution of the ambient and driven reflections. Finally, the Fe/sapphire interface velocity was monitored using a line-imaging VISAR with a field of view of 400 μm .

The synchronization of the main optical beam with the XFEL beam was performed in the same way as described by Albertazzi, et al.⁷¹ and whose dynamics are discussed by Hartley, et al.⁷² The coarse timing is tuned with a photodiode that measures emission from a polyimide sample. Fine tuning is accomplished with a 500 nm thick polycrystalline Au sample. The timing baseline, i.e., zero probe delay, is defined as the time when the diffraction from the Au sample begins to broaden due to sample heating.

Hydrodynamic Simulations

Simulations are performed with the incident laser pulse profile and measured target layers. Figure 6 shows the simulated pressure as a function of time and Lagrangian space for peak irradiance of 8×10^{11} W/cm². We find a good match for a lower irradiance than used in the experiment, which is typical for 1D simulations. The location of the CH, Fe, and sapphire layers are indicated on the bottom. We used the SESAME 2150 equation of state tables⁷³ for pure Fe and a QEOS⁶⁰ equation of state for Fe-Si_{16wt%}. Here we observe a complicated wave interaction due to surface reflections in the multi-layer sample. However, the short attenuation length of 10.1 keV X-rays in Fe (7.46 μm) and the oblique probe angle heavily bias our recorded signal to a small volume near the Fe/sapphire interface with $\sim 64\%$ of the signal coming from a depth of 1 μm (normal to the Fe/sapphire interface surface). This is consistent with the lack of gradients or asymmetry seen in the diffraction.

Density Functional Theory

For each of the Fe₁₀Si₂, Fe₅Si₂ and Fe₁₀Si₄ crystalline cells, 10,000 random structures have been generated. These random structures were generated with the AIRSS code⁶⁷ by imposing a minimum interatomic distance of 1.5 Å and were comprised in the volume range between 7 - 14 Å³/atom. At each desired pressure, the enthalpy $H=U+P_{ext} \times V$ where U is the internal energy, P_{ext} is the externally-applied pressure, and V is the volume, of the initial random structures was calculated with the Quantum ESPRESSO

ab-initio code^{74;75}, as a preliminary indication of their likely thermodynamic favorability. The 1% of the structures with the lowest initial enthalpy were selected for further processing. These favorable structures were subsequently clustered using Daura's algorithm⁷⁶ (cutoff value of 2.5) based on the PIV metric⁷⁷ with a switching function decaying from 0.9 to 0.1 between 1 and 6 Å. This clustering resulted in a few tens of cluster centers: the geometry of such atomic configurations was optimized with a precision better than 1 meV to obtain the final structures and enthalpies. We adopted the following parameters for DFT calculations: PBE exchange-correlation functional, ultra-soft Vanderbilt pseudopotentials, kinetic-energy cutoff = 60 Ry, charge density cutoff = 600 Ry, $8 \times 8 \times 8$ k-point grid, and Methfessel-Paxton smearing with width = 0.01 Ry.

The identity of the final relaxed phases was confirmed with three different methods: space group and symmetry assignment using the spglib library⁷⁸, enthalpy equivalence between structures, and structure factor comparison calculated using the VESTA crystal visualization software package⁷⁹. The appearance of the crystal structures was also visualized and inspected with VESTA.

Data Availability

Data that support the findings are available from the corresponding author upon request.

References

1. Poirier, J.-P. Light Elements in the Earth's Outer Core: A Critical Review. *Physics of the Earth and Planetary Interiors* **85**, 319–337 (1994). URL <https://www.sciencedirect.com/science/article/pii/0031920194901201?via%3Dihub>.
2. Badro, J. *et al.* Effect of Light Elements on the Sound Velocities in Solid Iron: Implications For the Composition of Earth's Core. *Earth and Planetary Science Letters* **254**, 233–238 (2007). URL <https://www.sciencedirect.com/science/article/pii/S0012821X06008405>.
3. McDonough, W. F. Compositional Model for the Earth's Core. *Treatise On Geochemistry* 547–568 (2003). URL <https://www.sciencedirect.com/science/article/pii/B0080437516020156>.
4. Antonangeli, D. *et al.* Composition of the Earth's Inner Core From High-Pressure Sound Velocity Measurements in Fe–Ni–Si Alloys. *Earth and Planetary Science Letters* **295**, 292–296 (2010). URL <http://dx.doi.org/10.1016/j.epsl.2010.04.018>.
5. Mao, Z. *et al.* Sound Velocities of Fe and Fe-Si Alloy in the Earth's Core. *Proceedings of the National Academy of Sciences* **109**, 10239–10244 (2012). URL <https://www.pnas.org/content/109/26/10239>.
6. Fischer, R. a. *et al.* Equation of State and Phase Diagram of Fe-16Si Alloy as a Candidate Component of Earth's Core. *Earth and Planetary Science Letters* **357-358**, 268–276 (2012). URL <http://dx.doi.org/10.1016/j.epsl.2012.09.022>.
7. Fei, Y., Murphy, C., Shibazaki, Y., Shahar, A. & Huang, H. Thermal Equation of State of hcp-Iron: Constraint on the Density Deficit of Earth's Solid Inner Core. *Geophysical Research Letters* **43**, 6837–6843 (2016). URL <https://agupubs.onlinelibrary.wiley.com/doi/full/10.1002/2016GL069456>.

8. Miozzi, F. *et al.* A New Reference for the Thermal Equation of State of Iron. *Minerals* **10**, 100 (2020). URL <https://www.mdpi.com/2075-163X/10/2/100>.
9. Knittle, E. & Jeanloz, R. Earth's Core-Mantle Boundary: Results of Experiments at High Pressures and Temperatures. *Science* **251**, 1438–1443 (1991). URL <https://science.sciencemag.org/content/251/5000/1438>.
10. Goarant, F., Guyot, F., Peyronneau, J. & Poirier, J.-P. High-pressure and High-Temperature Reactions Between Silicates and Liquid Iron Alloys, in the Diamond Anvil Cell, Studied by Analytical Electron Microscopy. *Journal of Geophysical Research: Solid Earth* **97**, 4477–4487 (1992). URL <https://agupubs.onlinelibrary.wiley.com/doi/abs/10.1029/92JB00018>.
11. Caracas, R. & Wentzcovitch, R. Equation of State and Elasticity of FeSi. *Geophysical Research Letters* **31**, L20603 (2004). URL <https://agupubs.onlinelibrary.wiley.com/doi/abs/10.1029/2004GL020601>.
12. Malavergne, V., Toplis, M. J., Berthet, S. & Jones, J. Highly Reducing Conditions During Core Formation on Mercury: Implications for Internal Structure and the Origin of a Magnetic Field. *Icarus* **206**, 199 – 209 (2010). URL <http://www.sciencedirect.com/science/article/pii/S0019103509003790>.
13. Hauck II, S. A. *et al.* The Curious Case of Mercury's Internal Structure. *Journal of Geophysical Research: Planets* **118**, 1204–1220 (2013). URL <https://agupubs.onlinelibrary.wiley.com/doi/abs/10.1002/jgre.20091>.
14. Malavergne, V. *et al.* How Mercury Can be the Most Reduced Terrestrial Planet and Still Store Iron in its Mantle. *Earth and Planetary Science Letters* **394**, 186 – 197 (2014). URL <http://www.sciencedirect.com/science/article/pii/S0012821X14001721>.
15. Chabot, N. L., Wollack, E. A., Klima, R. L. & Minitti, M. E. Experimental Constraints on Mercury's Core Composition. *Earth and Planetary Science Letters* **390**, 199 – 208 (2014). URL <http://www.sciencedirect.com/science/article/pii/S0012821X14000077>.
16. Exoplanet.eu. <http://exoplanet.eu/catalog/>. Accessed: 2020-04-28.
17. Unterborn, C. T., Dismukes, E. E. & Panero, W. R. Scaling the Earth: A Sensitivity Analysis of Terrestrial Exoplanetary Interior Models. *The Astrophysical Journal* **819**, 32 (2016). URL <https://doi.org/10.3847/2F0004-637x%2F819%2F1%2F32>.
18. Tateno, S., Hirose, K., Ohishi, Y. & Tatsumi, Y. The Structure of Iron in Earth's Inner Core. *Science* **330**, 359–361 (2010). URL <http://www.sciencemag.org/cgi/doi/10.1126/science.1194662>.
19. Gleason, A. E. & Mao, W. L. Strength of Iron at Core Pressures and Evidence for a Weak Earth's Inner Core. *Nature Geoscience* **6**, 571–574 (2013). URL <http://www.nature.com/articles/ngeo1808>.
20. Smith, R. F. *et al.* Time-Dependence of the Alpha to Epsilon Phase Transformation in Iron. *Journal of Applied Physics* **114**, 223507 (2013). URL <http://aip.scitation.org/doi/10.1063/1.4839655>.

21. Amadou, N. *et al.* Kinetics of the Iron $\alpha - \epsilon$ Phase Transition at High-Strain Rates: Experiment and Model. *Physical Review B* **93**, 214108 (2016). URL <http://link.aps.org/doi/10.1103/PhysRevB.93.214108>.
22. Kibaschewski, O. *Iron-Binary Phase Diagrams* (Springer-Verlag, 1982). URL <https://link.springer.com/book/10.1007%2F978-3-662-08024-5>.
23. Fischer, R. A. *et al.* Phase Relations in the Fe-FeSi System at High Pressures and Temperatures. *Earth and Planetary Science Letters* **373**, 54–64 (2013). URL <http://dx.doi.org/10.1016/j.epsl.2013.04.035>.
24. Wicks, J. K. *et al.* Crystal Structure and Equation of State of Fe-Si Alloys at Super-Earth Core Conditions. *Science Advances* **4** (2018). URL <http://advances.sciencemag.org/content/4/4/eaao5864>.
25. Edmund, E. *et al.* Structure and Elasticity of Cubic Fe-Si Alloys at High Pressures. *Physical Review B* **100**, 134105 (2019). URL <https://doi.org/10.1103/PhysRevB.100.134105>.
26. Antonangeli, D., Merkel, S. & Farber, D. L. Elastic Anisotropy in hcp Metals at High Pressure and the Sound Wave Anisotropy of the Earth's Inner Core. *Geophysical Research Letters* **33** (2006). URL <https://agupubs.onlinelibrary.wiley.com/doi/abs/10.1029/2006GL028237>.
27. Woodhouse, J. H., Giardini, D. & Li, X.-D. Evidence for Inner Core Anisotropy From Free Oscillations. *Geophysical Research Letters* **13**, 1549–1552 (1986). URL <http://doi.wiley.com/10.1029/GL013i013p01549>.
28. Morelli, A., Dziewonski, A. M. & Woodhouse, J. H. Anisotropy of the Inner Core Inferred From PKIKP Travel Times. *Geophysical Research Letters* **13**, 1545–1548 (1986). URL <http://doi.wiley.com/10.1029/GL013i013p01545>.
29. Stixrude, L. & Cohen, R. E. High-Pressure Elasticity of Iron and Anisotropy of Earth's Inner Core. *Science* **267**, 1972–1975 (1995). URL <http://www.sciencemag.org/cgi/doi/10.1126/science.267.5206.1972>.
30. Belonoshko, A., Skorodumova, N., Rosengren, A. & Johansson, B. Elastic Anisotropy of Earth's Inner Core. *Science* **319**, 797–800 (2008). URL <http://science.sciencemag.org/content/319/5864/797.full>.
31. Huntington, C. M. *et al.* Investigating Iron Material Strength up to 1 Mbar Using Rayleigh-Taylor Growth Measurements. *AIP Conference Proceedings* **1793**, 110007 (2017). URL <http://aip.scitation.org/doi/abs/10.1063/1.4971670>.
32. Krygier, A. *et al.* Extreme Hardening of Pb at High Pressure and Strain Rate. *Physical Review Letters* **123**, 205701 (2019). URL <https://doi.org/10.1103/PhysRevLett.123.205701>.
33. Hirao, N., Ohtani, E., Kondo, T. & Kikegawa, T. Equation of State of Iron-Silicon Alloys to Megabar Pressure. *Physics and Chemistry of Minerals* **31**, 329–336 (2004). URL <https://link.springer.com/article/10.1007/s00269-004-0387-x>.

34. Morrison, R. A., Jackson, J. M., Sturhahn, W., Zhang, D. & Greenberg, E. Equations of State and Anisotropy of Fe-Ni-Si Alloys. *Journal of Geophysical Research: Solid Earth* **123**, 4647–4675 (2018). URL <https://agupubs.onlinelibrary.wiley.com/doi/abs/10.1029/2017JB015343>.
35. Edmund, E. *et al.* Axial Compressibility and Thermal Equation of State of Hcp Fe–5wt% Ni–5wt% Si. *Minerals* **10**, 98 (2020). URL <http://dx.doi.org/10.3390/min10020098>.
36. Dubrovinsky, L., Dubrovinskaia, N., Prakpenka, V. B. & Abakumov, A. M. Implementation of Micro-Ball Nanodiamond Anvils for High-Pressure Studies Above 6 Mbar. *Nature Communications* **3**, 1163 (2012). URL <https://www.nature.com/articles/ncomms2160>.
37. Morard, G. *et al.* Solving Controversies on the Iron Phase Diagram Under High Pressure. *Geophysical Research Letters* **45**, 11,074–11,082 (2018). URL <https://agupubs.onlinelibrary.wiley.com/doi/abs/10.1029/2018GL079950>.
38. Okamoto, H. The C-Fe (Carbon-Iron) System. *Journal of Phase Equilibria* **13**, 543–565 (1992). URL <https://doi.org/10.1007/BF02665767>.
39. Verhoogen, J. Phase Changes and Convection in the Earth’s Mantle. *Philosophical Transactions of the Royal Society of London. Series A, Mathematical and Physical Sciences* **258**, 276–283 (1965). URL <https://royalsocietypublishing.org/doi/abs/10.1098/rsta.1965.0040>.
40. Merkel, S., Miyajima, N., Antonangeli, D., Fiquet, G. & Yagi, T. Lattice Preferred Orientation and Stress in Polycrystalline hcp-Co Plastically Deformed Under High Pressure. *Journal of Applied Physics* **100**, 0–8 (2006). URL <https://aip.scitation.org/doi/10.1063/1.2214224>.
41. Barker, L. M. & Hollenbach, R. E. Shock wave study of the $\alpha \rightleftharpoons \epsilon$ phase transition in iron. *Journal of Applied Physics* **45**, 4872–4887 (1974). URL <http://aip.scitation.org/doi/10.1063/1.1663148>.
42. Jensen, B. J., Gray, G. T. & Hixson, R. S. Direct Measurements of the Alpha Epsilon Transition Stress and Kinetics for Shocked Iron. *Journal of Applied Physics* **105** (2009). URL <https://aip.scitation.org/doi/10.1063/1.3110188>.
43. Gleason, A. E. *et al.* Ultrafast Visualization of Crystallization and Grain Growth in Shock-Compressed SiO₂. *Nature Communications* **6**, 8191 (2015). URL <http://www.nature.com/doi/abs/10.1038/ncomms9191>.
44. Langrand, C. *et al.* Kinetics and Detectability of the Bridgmanite to Post-Perovskite Transformation in the Earth’s D” Layer. *Nature Communications* **10**, 5680 (2019). URL <https://doi.org/10.1038/s41467-019-13482-x>.
45. McBride, E. E. *et al.* Phase Transition Lowering in Dynamically Compressed Silicon. *Nature Physics* (2018). URL <http://www.nature.com/articles/s41567-018-0290-x>.
46. Coleman, A. L. *et al.* Identification of Phase Transitions and Metastability in Dynamically Compressed Antimony Using Ultrafast X-Ray Diffraction. *Phys. Rev. Lett.* **122**, 255704 (2019). URL <https://link.aps.org/doi/10.1103/PhysRevLett.122.255704>.

47. Ishikawa, T. *et al.* A Compact X-ray Free-Electron Laser Emitting in the Sub-Angstrom Region. *Nature Photonics* **6**, 540–544 (2012). URL <https://www.nature.com/articles/nphoton.2012.141>.
48. Tono, K. *et al.* Beamline, experimental stations and photon beam diagnostics for the hard X-ray free electron laser of SACLA. *New Journal of Physics* **15**, 083035 (2013). URL <http://iopscience.iop.org/article/10.1088/1367-2630/15/8/083035/meta>.
49. Inubushi, Y. *et al.* Development of an Experimental Platform for Combinative Use of an XFEL and a High-Power Nanosecond Laser. *Applied Sciences* **10** (2020). URL <https://www.mdpi.com/2076-3417/10/7/2224>.
50. Fat'yanov, O. V., Webb, R. L. & Gupta, Y. M. Optical Transmission Through Inelastically Deformed Shocked Sapphire: Stress and Crystal Orientation Effects. *Journal of Applied Physics* **97**, 123529 (2005). URL <https://doi.org/10.1063/1.1937470>.
51. Ramis, R., Schmalz, R. & Meyer-Ter-Vehn, J. MULTI — A Computer Code for One-Dimensional Multigroup Radiation Hydrodynamics. *Computer Physics Communications* **49**, 475 – 505 (1988). URL <http://www.sciencedirect.com/science/article/pii/0010465588900082>.
52. Brown, J. M., Fritz, J. N. & Hixson, R. S. Hugoniot Data for Iron. *Journal of Applied Physics* **88**, 5496–5498 (2000). URL <http://aip.scitation.org/doi/10.1063/1.1319320>.
53. Hawreliak, J. A. *et al.* In Situ X-ray Diffraction Measurements of the c/a Ratio in the High-Pressure ϵ Phase of Shock-Compressed Polycrystal Iron. *Physical Review B* **83**, 144114 (2011). URL <http://link.aps.org/doi/10.1103/PhysRevB.83.144114>.
54. Mao, H. K., Wu, Y., Chen, L. C., Shu, J. F. & Jephcoat, A. P. Static Compression of Iron To 300 GPa and Fe_{0.8}Ni_{0.2} Alloy to 260 GPa: Implications for Composition of the Core. *Journal of Geophysical Research* **95**, 21737 (1990). URL <http://doi.wiley.com/10.1029/JB095iB13p21737>.
55. Kalantar, D. H. *et al.* Direct Observation of the α - ϵ Transition in Shock-Compressed Iron via Nanosecond X-ray Diffraction. *Physical Review Letters* **95**, 1–4 (2005). URL <https://journals.aps.org/prl/abstract/10.1103/PhysRevLett.95.075502>.
56. Dewaele, A. *et al.* Mechanism of the α - ϵ Phase Transformation in Iron. *Physical Review B* **91**, 174105 (2015). URL <http://link.aps.org/doi/10.1103/PhysRevB.91.174105>.
57. McGonegle, D., Milathianaki, D., Remington, B. A., Wark, J. S. & Higginbotham, A. Simulations of In Situ X-ray Diffraction From Uniaxially Compressed Highly Textured Polycrystalline Targets. *Journal of Applied Physics* **118**, 065902 (2015). URL <http://dx.doi.org/10.1063/1.4927275><http://aip.scitation.org/doi/10.1063/1.4927275>.
58. Polsin, D. N. *et al.* Measurement of Body-Centered-Cubic Aluminum at 475 GPa. *Physical Review Letters* **119**, 175702 (2017). URL <https://journals.aps.org/prl/abstract/10.1103/PhysRevLett.119.175702>.
59. Ohnuma, I. *et al.* Experimental and Thermodynamic Studies of the Fe-Si Binary System. *ISIJ International* **52**, 540–548 (2012). URL https://www.jstage.jst.go.jp/article/isijinternational/52/4/52_4_540/_article/-char/en.

60. More, R. M., Warren, K. H., Young, D. A. & Zimmerman, G. B. A New Quotidian Equation of State (QEOS) For Hot Dense Matter. *The Physics of Fluids* **31**, 3059 (1988). URL <https://doi.org/10.1063/1.866963>.
61. Marsh, S. P. *LASL shock Hugoniot data*, vol. 5 (Univ of California Press, 1980).
62. Kadau, K., Germann, T. C., Lomdahl, P. S. & Holian, B. L. Atomistic simulations of shock-induced transformations and their orientation dependence in bcc Fe single crystals. *Physical Review B - Condensed Matter and Materials Physics* **72** (2005). URL <https://journals.aps.org/prb/abstract/10.1103/PhysRevB.72.064120>.
63. Kadau, K. *et al.* Shock Waves in Polycrystalline Iron. *Physical Review Letters* **98**, 1–4 (2007). URL <https://journals.aps.org/prl/abstract/10.1103/PhysRevLett.98.135701>.
64. Fischer, R. A. & Campbell, A. J. The Axial Ratio of hcp Fe and Fe-Ni-Si Alloys to the Conditions of Earth's Inner Core. *American Mineralogist* **100**, 2718–2724 (2015). URL <https://doi.org/10.2138/am-2015-5191>.
65. Edmund, E. *et al.* Velocity-Density Systematics of Fe-5wt%Si : Constraints on Si Content in the Earth's Inner Core. *Journal Geophysical Research: Solid Earth* **124**, 3436 (2019). URL <https://agupubs.onlinelibrary.wiley.com/doi/abs/10.1029/2018JB016904>.
66. Perdew, J. P., Burke, K. & Ernzerhof, M. Generalized Gradient Approximation Made Simple. *Phys. Rev. Lett.* **77**, 3865–3868 (1996). URL <https://link.aps.org/doi/10.1103/PhysRevLett.77.3865>.
67. Pickard, C. J. & Needs, R. J. Ab Initio Random Structure Searching. *Journal of Physics: Condensed Matter* **23**, 053201 (2011). URL <https://doi.org/10.1088%2F0953-8984%2F23%2F5%2F053201>.
68. Mogni, G. private communication (2020).
69. Lin, J.-f., Heinz, D. L. & Campbell, A. J. Iron-Silicon Alloy in Earth's Core? *Science* **295**, 313–315 (2002). URL <https://science.sciencemag.org/content/295/5553/313>.
70. Prescher, C. & Prakapenka, V. B. DIOPTAS: A Program for Reduction of Two-Dimensional X-ray Diffraction Data and Data Exploration. *High Pressure Research* **7959** (2015). URL <https://doi.org/10.1080/08957959.2015.1059835>.
71. Albertazzi, B. *et al.* Dynamic Fracture of Tantalum Under Extreme Tensile Stress. *Science Advances* **3**, 1–7 (2017). URL <http://advances.sciencemag.org/content/3/6/e1602705.abstract>.
72. Hartley, N. J. *et al.* Ultrafast Observation of Lattice Dynamics in Laser-Irradiated Gold Foils. *Applied Physics Letters* **110**, 071905 (2017). URL <http://dx.doi.org/10.1063/1.4976541>.
73. Kerley, G. I. Multiphase Equation of State for Iron. *Sandia Report SAND93*, 0027 (1993).

74. Giannozzi, P. *et al.* QUANTUM ESPRESSO: A Modular and Open-Source Software Project for Quantum Simulations of Materials. *Journal of Physics: Condensed Matter* **21**, 395502 (2009). URL <https://doi.org/10.1088%2F0953-8984%2F21%2F39%2F395502>.
75. Giannozzi, P. *et al.* Advanced Capabilities for Materials Modeling with Quantum ESPRESSO. *Journal of Physics: Condensed Matter* **29**, 465901 (2017). URL <https://doi.org/10.1088%2F1361-648x%2Faa8f79>.
76. Daura, X. *et al.* Peptide Folding: When Simulation Meets Experiment. *Angewandte Chemie International Edition* **38**, 236–240 (1999). URL [https://doi.org/10.1002/\(SICI\)1521-3773\(19990115\)38:1/2%3C236::AID-ANIE236%3E3.0.CO;2-M](https://doi.org/10.1002/(SICI)1521-3773(19990115)38:1/2%3C236::AID-ANIE236%3E3.0.CO;2-M).
77. Gallet, G. A. & Pietrucci, F. Structural Cluster Analysis of Chemical Reactions in Solution. *The Journal of Chemical Physics* **139**, 074101 (2013). URL <https://doi.org/10.1063/1.4818005>.
78. Togo, A. & Tanaka, I. Spglib: A Software Library for Crystal Symmetry Search (2018). 1808.01590.
79. Momma, K. & Izumi, F. VESTA3 for Three-Dimensional Visualization of Crystal, Volumetric and Morphology Data. *Journal of Applied Crystallography* **44**, 1272–1276 (2011). URL <https://doi.org/10.1107/S0021889811038970>.

Figures

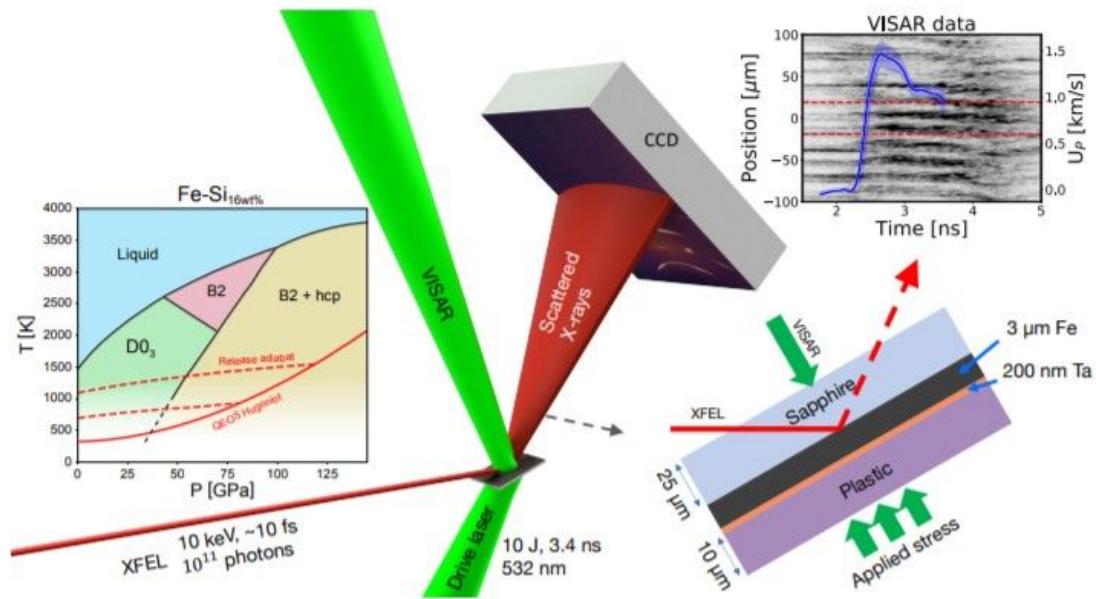


Figure 1

The experimental setup and sample VISAR data. A CCD detector located 76 mm from the interaction point and covering the range $2\theta_B = [17^\circ:100^\circ]$ collects scattered x-rays. The sandwich sample layers, shown in the bottom right, are 10 μm CH / 200 nm Ta / 3 μm Fe / 25 μm sapphire. On some shots, there was an additional 100 nm Au layer on the Sapphire window. The top right inset shows sample VISAR data with the XFEL probe region highlighted in dashed lines. The shaded region in the VISAR data shows the statistical standard deviation of the velocity. The inset to the left shows the Fe-Si_{16wt%} phase diagram from Fischer²³ with the shock Hugoniot and example QEOS release adiabats.

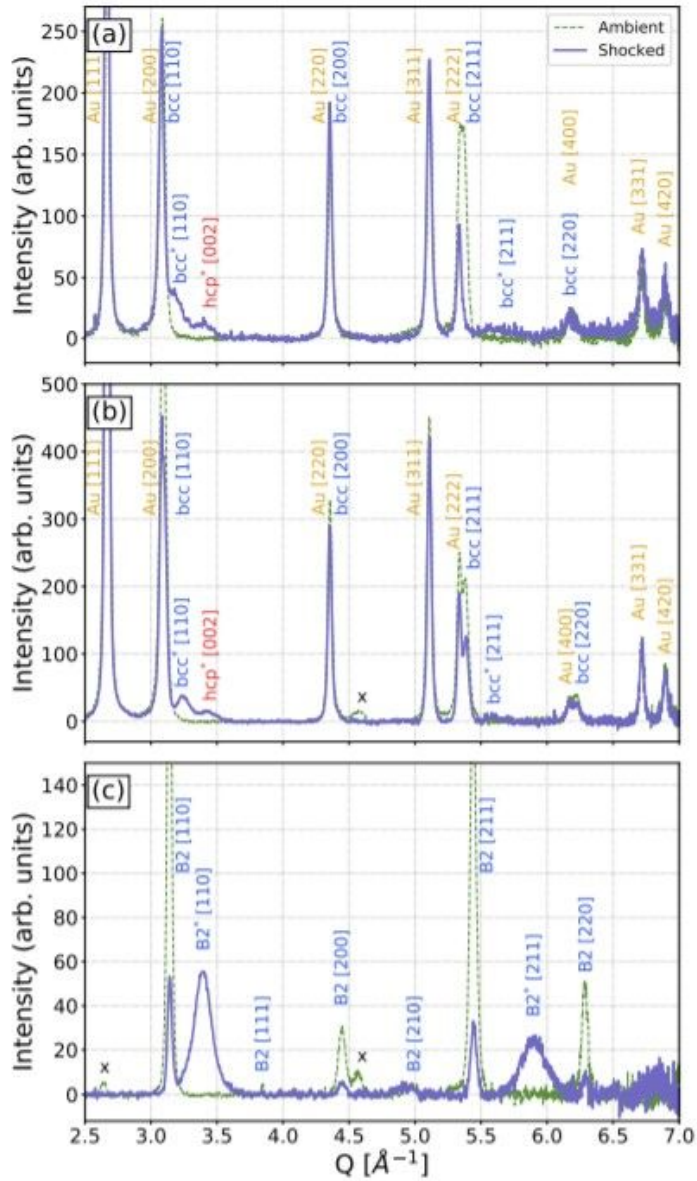


Figure 2

Azimuthally integrated diffraction patterns of shocked Fe (a), Fe-Si8.5wt% (b), and Fe-Si16wt% (c). Upon compression, Fe and Fe-Si8.5wt% form a mixture of bcc and hcp phases, respectively. Our data shows that Fe-Si16wt% stays in the cubic phase. The black x symbol in (b) and (c) indicates reflections from the sample holder. We have masked out reflections from the single crystal sapphire.

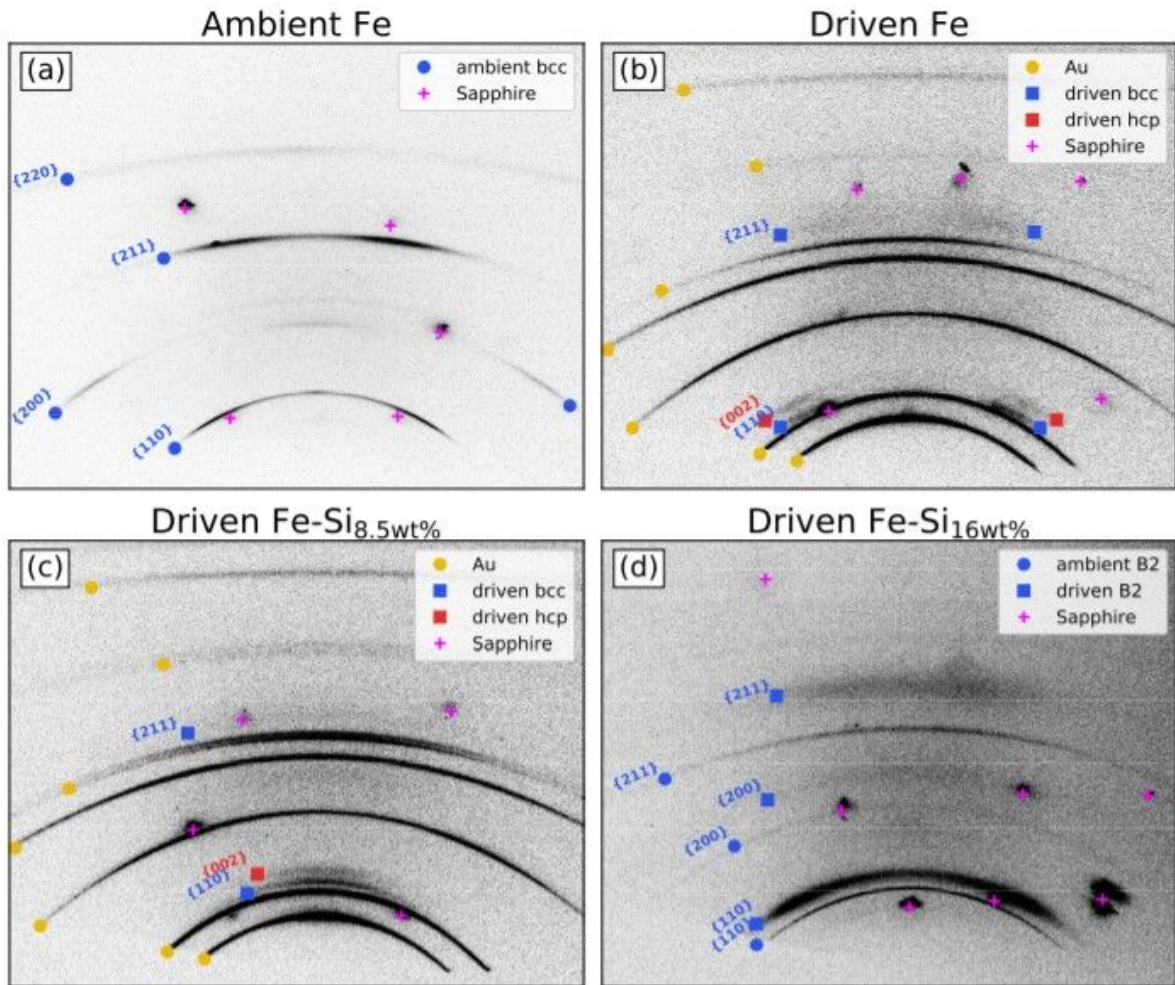


Figure 3

Raw diffraction images of ambient Fe (a), driven Fe (b), driven Fe-Si8.5wt% (c), and driven Fe-Si16wt% (d) with phases identified. The driven images correspond to the integrations shown in figure 2 and described in the text. Circles and squares indicate ambient and high-pressure reflections, respectively. Gold circles indicate Au reflections in (b) and (c); pink pluses indicate single crystal sapphire reflections. Blue and red markers indicate cubic (bcc/B2) hcp phase reflections blue and red, respectively. The ambient Fe image (a) clearly shows the initial sample texture; in (b) the Au obscures the ambient texture. The Debye-Scherrer rings form ellipses due to the geometry (see Fig. 1); the diffuse background is likely due to X-rays generated in the front-surface laser ablation and fluorescence from the XFEL interacting with the Au layer.

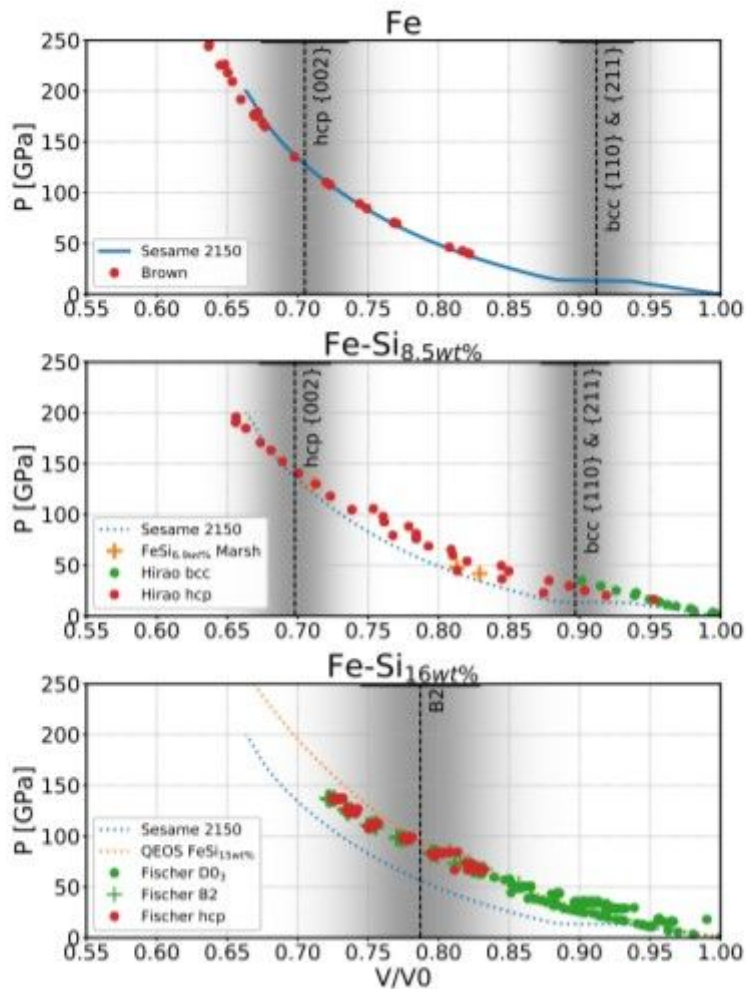


Figure 4

Pressure-volume relations for Fe, Fe-Si8.5wt%, and Fe-Si16wt% plotted with similar alloys. The black lines/gray shading show volume and uncertainty of our measurements. Comparative Hugoniot/static data: in (a), the Sesame 2150 calculated shock Hugoniot is plotted with shock Hugoniot data from Brown et al.⁵²; in (b), static compression phase relation data for Fe-Si8.7wt% from Hirao et al.³³ taken at 300 K and shock Hugoniot data for Fe-Si6.9wt% from Marsh et al.⁶¹ are plotted; in (c), static compression data for Fe-Si16wt% from Fischer et al.²³ heated between 300-2200 K. Panels (b) and (c) also show the Sesame 2150 shock Hugoniot for comparison.

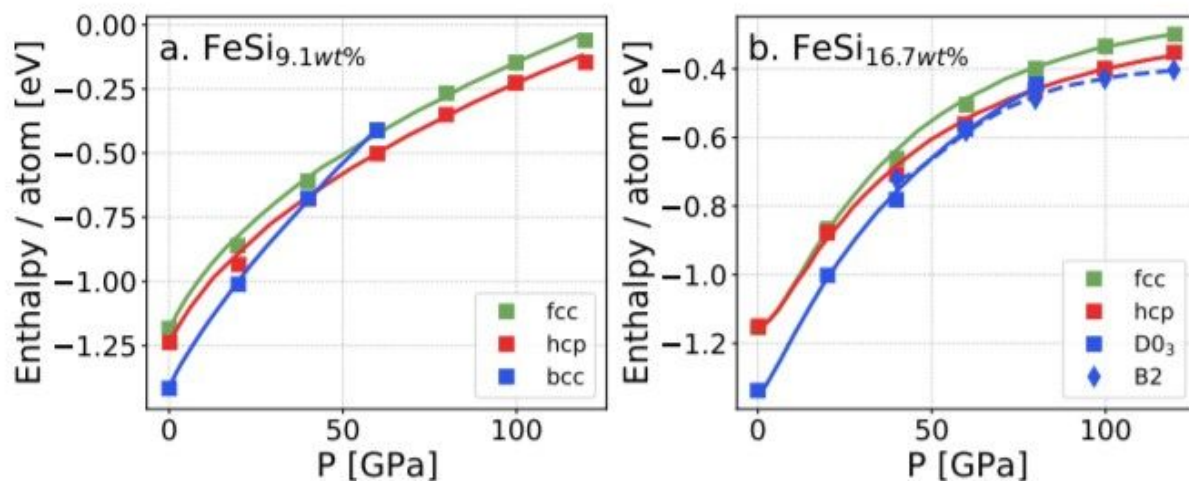


Figure 5

Phase stability calculations using density functional theory at 0 K for Fe-Si_{9.1wt%} (a) and Fe-Si_{16.7wt%} (b).

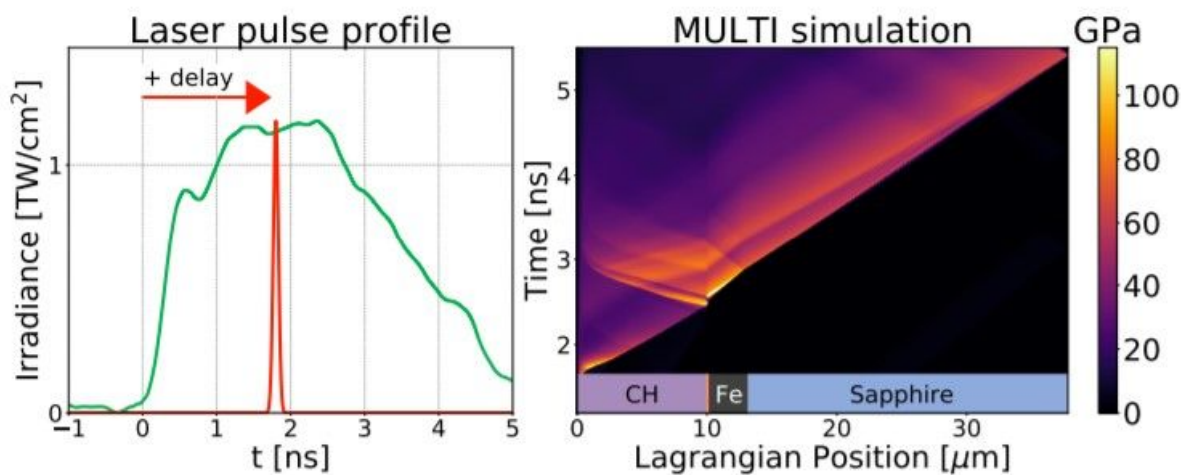


Figure 6

Experimental pulse shape (left panel) and MULTI hydrodynamics (right panel) simulation showing the pressure as a function of time and Lagrangian position. The peak irradiance is 8×10^{11} W/cm², which is lower than our experimental irradiance as typical of 1D radiation hydrodynamics simulations, produces the best fit to our data. The sample layers are indicated on the bottom (with the Ta heat shield included, but not labeled).